Linking feldspar luminescence phenomena and mineralogy using spatially resolved techniques

RIEDESEL, Svenja, DULLER, Geoff A. T., HELLERS, Max, PEARCE, Nick J. G., WINZAR, Joseph A., BELL, Anthony <http://orcid.org/0000-0001-5038-5621> and KLEINSCHRODT, Reiner

---

This document is the Published Version [VoR]

Citation:

RIEDESEL, Svenja, DULLER, Geoff A. T., HELLERS, Max, PEARCE, Nick J. G., WINZAR, Joseph A., BELL, Anthony and KLEINSCHRODT, Reiner (2026). Linking feldspar luminescence phenomena and mineralogy using spatially resolved techniques. Physics and Chemistry of Minerals, 53 (2): 8. [Article]

Physics and Chemistry of Minerals (2026) 53:8
https://doi.org/10.1007/s00269-026-01345-z

ORIGINAL PAPER

Linking feldspar luminescence phenomena and mineralogy using spatially resolved techniques

Svenja Riedesel[1] · Geoff A. T. Duller[2] · Max Hellers[3] · Nick J. G. Pearce[2] · Joseph A. Winzar[2] · Anthony M. T. Bell[4] · Reiner Kleinschrodt[3]

Received: 23 September 2025 / Accepted: 19 February 2026

Abstract

Feldspars, the most abundant mineral group in the Earth's crust, exhibit a striking chemical and structural variety resulting from variations in their crystallisation environments and post-crystallisation processes. Since feldspars record both formation and alteration processes and conditions, they are key components in geological studies and valuable for developing tools to reconstruct past environmental change. Thermally and optically stimulated luminescence, the ability of minerals, such as feldspars, to emit light in different wavelengths upon excitation with light or heat, are sensitive to changes in the crystal lattice and thus may have the potential to be used as a tool for identifying crystallisation and alteration processes affecting feldspars. So far, the luminescence of feldspars has primarily been used as a numerical geochronological dating technique, constraining past geological and archaeological events and processes. However, the sensitivity of feldspar luminescence signals to changes in crystallisation and post-crystallisation processes allows for the development of luminescence-based proxies beyond geochronological studies.

This study investigates the relationship between luminescence emission intensities in three emission bands and mineralogical features in 13 alkali feldspars and plagioclases using spatially resolved luminescence techniques, electron microprobe analysis, bulk geochemistry, and X-ray powder diffraction. The intensity of infrared photoluminescence (IRPL) emission (~900 and ~950 nm) is particularly sensitive to chemical and structural heterogeneities within the feldspar samples, such as the presence of K-rich phases, fractures, and alteration products. Blue (~400 nm) thermoluminescence (TL) and infrared stimulated luminescence (IRSL) emission intensities vary with feldspar type and perthitic texture, while yellow-green (~560 nm) TL and IRSL emissions are linked to fluid-induced alteration of the feldspar chemistry and structure. These findings highlight the potential of spatially resolved luminescence measurements as a non-destructive tool for identifying crystallisation and alteration processes in feldspars, as well as relationships between luminescence signal intensity and mineralogical properties, advancing both geochronological techniques which use these emissions, and mineralogical studies.

Keywords Feldspar · Luminescence · Electron microprobe · Geochemistry · Alteration

Introduction

Feldspars are the most abundant mineral group in the Earth's crust, and a major constituent of igneous, and metamorphic rocks, and the sediments derived from these. Their ubiquity makes them an important target for many geological, petrological, and geomorphological studies into the formation of the Earth's surface. Feldspars exhibit a vast chemical and structural variety that forms during crystallisation and is affected by alteration processes. The responsiveness of feldspars to record their crystallisation environment, as well as alteration processes, such as fluid interactions or weathering

✉ Svenja Riedesel
svenja.riedesel@uni-koeln.de

[1] Institute of Geography, University of Cologne, 50674 Cologne, Germany

[2] Department of Geography and Earth Sciences, Aberystwyth University, Aberystwyth SY23 3DB, UK

[3] Institute of Geology and Mineralogy, University of Cologne, 50674 Cologne, Germany

[4] Materials and Engineering Research Institute, Sheffield Hallam University, Sheffield S1 1WB, UK

(e.g. Chardon et al. 2006; Hangx and Spier 2009; Yuan et al. 2019; Hellmann et al. 2021), makes these minerals the ideal target to develop novel tools for quantifying past environmental changes.

Feldspars have been used to constrain crystallisation and cooling rates (e.g. Stormer 1975; Brown and Parsons 1981; Kroll et al. 1993; Gorelova et al. 2023), and to trace origins and flow paths of hydrothermal fluids (e.g. Frank et al. 2019; Duan et al. 2021). Weathering of silicates, such as feldspars, is understood as one of the main processes removing CO_2 from the atmosphere, controlling the Earth's atmospheric composition and temperature (e.g. Goudie and Viles 2012; Brantley et al. 2023). Thus, developing tools to gain insight into crystallisation and alteration processes in feldspars is important for many geological, petrological, and geographical areas of study.

Traditionally, feldspar formation and post-crystallisation processes have been investigated using X-ray diffraction (XRD), electron probe microanalysis (EPMA), electron backscatter imagery (e.g. Harlov et al. 1998), scanning electron microscopy (SEM, e.g. Berner and Holdren 1977), transmission electron microscopy (TEM, e.g. Hellmann et al, 2021), energy-filtered transmission electron microscopy (e.g. Yuan et al. 2019), and cathodoluminescence (CL) (e.g. Richter et al. 2003; Kayama et al. 2010). The last technique (CL) utilises the ability of feldspars to store charge within defects in their crystalline structure, and studies have demonstrated that it can be used to investigate the presence of defects and trace elements within feldspars (e.g. Finch and Klein 1999). Related, but distinct types of luminescence from CL are infrared stimulated luminescence (IRSL, Hütt et al. 1988; Godfrey-Smith et al. 1988; Thomsen et al. 2008), thermoluminescence (TL, Aitken 1985) and infrared photoluminescence (IRPL, Prasad et al. 2017). These signals are stimulated either by heating (TL) or optically by wavelengths between the UV and near-IR (optically stimulated luminescence, OSL, and IRSL, as well as IRPL), rather than through interaction with an electron beam, such as in the case of CL, and have been widely studied because of their use in the fields of luminescence dating and dosimetry (e.g. Aitken 1985; Huntley 1985; Hütt et al. 1988; see Duller 2004; and Rhodes 2011 for a review). Whereas IRPL probes the excitation and subsequent retrapping of trapped electrons in the feldspar lattice non-destructively (Prasad et al. 2017), TL, OSL and IRSL are the result of electron-hole recombination (e.g. Duller 1997 for a review; Poolton et al. 2009; Jain and Ankjærgaard 2011). Whilst these processes are fairly well understood, the physical defects involved in these signals, and how they are influenced by feldspar structural and chemical characteristics are still contested (see e.g. Krbetschek et al. 1997; Riedesel et al. 2023; Williams and Spooner 2025). Improving our understanding of how different emissions from feldspars are influenced by their structural and chemical characteristics could make their application to investigating crystallisation, alteration, and weathering processes in feldspar possible.

Imaging detectors such as electron multiplying charge coupled devices (EMCCD) have been used to show that luminescence signals from individual grains of feldspar, or even from parts of these grains, have spatially heterogeneous sensitivity to radiation dose (e.g. Duller et al. 1997; Greilich et al. 2002; Baril 2004; Thomsen et al. 2018). Baril (2004) found relationships between different feldspar emissions and chemically different phases of a feldspar sample, and that the luminescence intensity varies significantly from sample to sample, based on their chemical composition. Thomsen et al. (2018) showed that the emission intensity of differently stimulated feldspar luminescence signals (TL, IRSL, post-IR IRSL, and IRPL) vary spatially across the samples examined and seems to be related to chemical variations within feldspar grains. Based on a limited number of feldspar samples, these studies already indicate the spatial heterogeneity of feldspar luminescence and thus imply the potential utility of spatially resolved luminescence as a tool to characterise chemically and structurally different feldspars.

This study explores the relationships between blue (~400 nm) and yellow-green (~560 nm) IRSL and TL signals, as well as IRPL signal (900 and 950 nm) and feldspar chemistry and structure using spatially resolved measurements of 13 feldspar samples with the aim of evaluating the potential for such techniques to be used for identifying crystallisation and alteration processes in feldspars.

Materials and methods

Sample information and bulk chemical and structural analyses

To investigate the role of chemistry and structure on feldspar IRSL, TL, and IRPL signals, 13 feldspar specimens that represent the wide range of feldspar minerals were used. The samples were prepared by cutting ~0.5 mm thin slices of larger feldspar samples using a cooled Buehler Isomet 1000 precision saw. The slices were cleaned in acetone to remove residues from the cutting process. Due to their irregular form, individual sample slices have diameters ranging from ~2 mm to ~8 mm depending on the grain axis measured.

The bulk chemistry and mineral phases present within the specimens were determined using X-ray fluorescence (XRF) and XRD, respectively. The results are given in Table 1; Fig. 1, and in more detail in Table S1 in the supplementary material. For XRF measurements 100 mg of

Table 1 Geochemical and mineralogical sample details

Sample ID	Origin	End member composition			Phases						Further details
		K-FS	Na-FS	Ca-FS	Microcline	Low sanidine	High sanidine	Albite	Anorthite	Quartz	
FSM-3	Toe Head, South Harris, Scotland, UK (Cunningham 1981)	82.5	17.2	0.3	78.0	-	-	22.0	-	-	microperthite, granite pegmatite source rock
FSM-5	Unknown	74.8	25.2	0.0	57.0	-	-	43.0	-	-	macroperthite
FSM-6	Trezaise Quarry, Cornwall, UK (Ussher et al. 1909)	74.4	25.3	0.3	-	38.0	-	62.0	-	-	microperthite, granite pegmatite source rock
FSM-15	Buckingham, Quebec, Canada	80.4	19.6	0.0	82.0	-	-	18.0	-	-	microperthite, metamorphically altered (or metasomatised)
CMFS-2	Volkesfeld, Eifel, Germany	90.9	8.83	0.23	97.0	-	-	-	-	3.0*	single phase
CMFS-5	Norway	76.9	22.4	0.67	70.0	30.0	-	-	-	-	microperthite
CMFS-6	Norway	79.3	19.9	0.77	59.0	41.0	-	-	-	-	microperthite
CMFS-8	unknown	88.6	11.2	0.15	-	76.0	-	24.0	-	-	macroperthite
CMFS-9	Landsverk, Norway	62.3	37.5	0.16	35.0	-	-	65.0	-	-	macroperthite
CMFS-12	Theriso, Crete, Greece	0.44	98.9	0.67	-	-	-	100.0	-	-	hydrothermally altered, single phase
CMFS-15	Norway	6.72	72.7	20.5	-	-	25.0	75.0	-	-	ternary FSP with K-FS patches
CMFS-16	Bjordammen, Norway	6.48	59.1	34.5	-	-	-	100.0**	-	-	plagioclase
CMFS-17	unknown	3.95	36.1	59.9	-	-	-	100.0**	-	-	single phase

The chemical composition as % of the feldspar end members was calculated from stoichiometric conversion using the semi-quantitative bulk XRF data. Mineral phases present in each sample were determined using semi-quantitative XRD-analyses. K-FS, Na-FS, and Ca-FS stand for K-feldspar, Na-feldspar and Ca-feldspar, respectively. *Likely a mineral inclusion. **Ca-bearing albite

powdered sample material was mixed with 100 mg of cellulose binder. This mixture was subsequently placed in Al sample boats. Each sample-containing Al-boat was pressed at 20 tons using a Retsch PP40 press to make pressed pellet samples suitable for XRF measurements using a PANalytical MagiX PRO XRF spectrometer equipped with a Rh anode X-ray source for the FSM samples. The MagiX PRO spectra were collected over ten different energy ranges and then analysed to obtain semi-quantitative results. XRF spectra for the CMFS samples were measured using a Rigaku Primus IV XRF spectrometer, also equipped with a Rh anode X-ray source. The Primus IV spectra were collected over twelve different energy ranges and then analysed to obtain semi-quantitative results. For the analyses, it was assumed that all elements, except for Cl, were present as oxides. The XRF results were used to calculate the individual sample compositions giving the molecular formula calculated based on stoichiometry assuming eight oxygens. The results are shown in Fig. 1a and given in Table 1.

For XRD measurements, 100 mg of powdered sample material was mounted on a low-background silicon XRD sample holder using acetone. The semi-quantitative XRD measurements were carried out on a PANalytical X'Pert MPD powder diffractometer at Sheffield Hallam University operating with Cu Kα X-rays and a PIXCEL-1D area detector. Data were collected over the range of 5–100° 2θ. The XRD results were used to perform semi-quantitative phase analyses by utilising the International Centre for Diffraction Data PDF-5+database, and the thus determined mineral phases are given in Table 1 and Table S2 in the supplementary material. Furthermore, the position and shape of the (131), $(13\bar{1})$, (060) and $(1\bar{1}1)$ diffraction peaks were used to determine the triclinicity and state of order of the alkali feldspars following Goldsmith and Laves (1954), Thompson

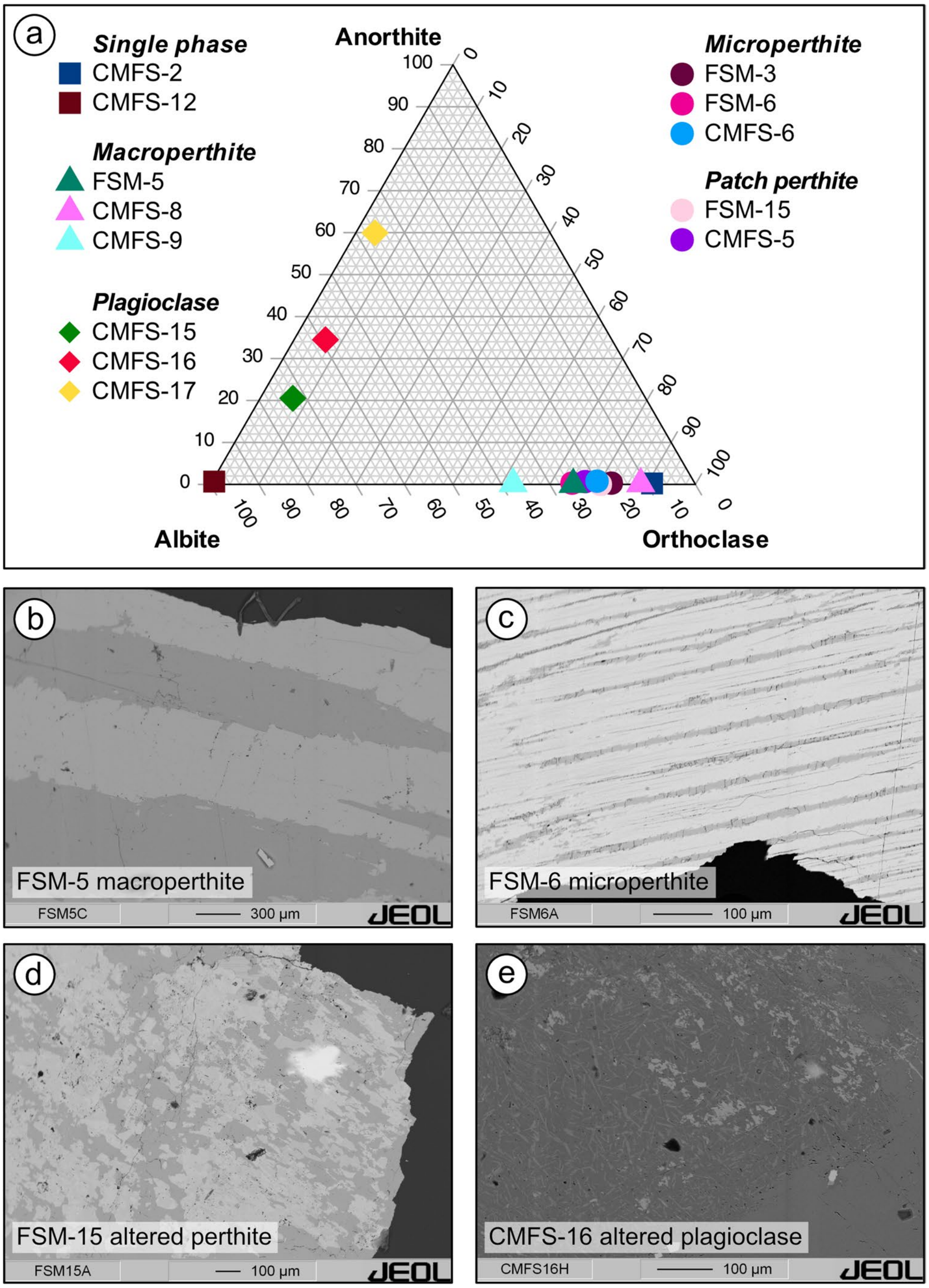

Fig. 1 Bulk XRF-based chemical composition of feldspar samples investigated (a) and electron back scatter images of selected samples (b-e)

(1969, 1970), and Hovis (1989). Thompson (1969, 1970) introduced the long-range ordering parameter Z, which was used to determine the state of order of all alkali feldspars in this study (see Table S2 for details). This characterisation revealed that the feldspar suite consisted of three plagioclase feldspars, nine alkali feldspars and one single-phase albite. The XRD results showed that the alkali feldspar sample suite includes a disordered high sanidine (CMFS-2), and a perthitic sample that contains an albite and a low sanidine phase. The remaining alkali feldspars are perthites with ordered microcline and albite phases.

Electron microprobe measurements

The chemistry of selected areas in each sample was determined using a JEOL JXA-8900RL Electron Microprobe Analyser (EMPA) housed at the Institute of Geology and Mineralogy (University of Cologne). Samples were embedded in colourless two component epoxy resin (Araldit 2020, Huntsman) and sanded and polished using 1200 SiO_2 sandpaper, and measurements were conducted with an accelerating voltage of 15 kV, a beam current and diameter of 15 nA and 1 µm, respectively. Elements were calibrated with mineral reference materials, and matrix-matched reference materials were analysed for quality control. Counting times on peak and on background were 20 s for Fe, Mn, and Ba, and 10 s for Si, Al, Ca, K, and Na. The ZAF method was applied for matrix correction, which includes the correction for the atomic number effect (Z), the absorption effect (A), and the fluorescence excitation effect (F) (e.g. Reed 2005). All measurements were performed as line scans, with points being measured every 5 µm, 10–20 µm, dependening on the sample and the feature of interest.

Electron backscatter images were taken of all samples to document specific mineralogical features and to determine where to start and end the line scans. Example electron backscatter images of four samples are shown in Figs. 1b-e. Electron backscatter images of all samples can be viewed in Figs. S13-S25 in the supplementary material.

Luminescence measurements

Luminescence measurements of three emission bands, infrared (IR, emissions at ~900 nm and ~950 nm), blue (~400 nm), and yellow-green (~560 nm), were performed using a modified Risø DA20 TL/OSL reader housed at the Aberystwyth Luminescence Research Laboratory (ALRL). The instrument is equipped with a $^{90}Sr/^{90}Y$ beta source, delivering ~0.1 Gy s^{-1} at the sample position, a detection and stimulation head (DASH, Lapp et al. 2015), and the sensitive infrared instrument for photo luminescence (SIRIOL, Gunn et al. 2022).

The DASH was used to perform TL and IRSL measurements, with emission detection of the blue (~400 nm) and yellow-green (~560 nm) emission bands. IRPL signals were detected at room temperature using SIRIOL. IR LEDs (˜850 nm, 175 mW cm^{-2}) mounted within the DASH were used for optical stimulation of IRSL, and an 830 nm laser diode (equipped with an 830 nm filter with a 10 nm bandwidth) housed within SIRIOL was used to stimulate IRPL using continuous wave stimulation. IRSL and TL signals were detected through either a combination of a 3 mm Schott BG39 and a 2 mm Schott BG3 filters or a combination of a 3 mm Schott BG39 and a 2 mm Schott OG550 filters, to isolate the blue (~400 nm) and yellow-green emission (~560 nm), respectively. Two IRPL emissions were isolated using two different filter combinations: A 900 nm long pass filter combined with a 900 nm band pass filter with a bandwidth of 50 nm was used to isolate the $IRPL_{900}$ emission and a 900 nm long pass filter combined with a 950 nm band pass filter with a bandwidth of 50 nm was used to isolate the $IRPL_{950}$ emission. Further information of the transmission of these filter combinations and the diode used for stimulation can be found in Gunn et al. (2022; see their Fig. 2 especially). Luminescence was detected using two Photometrics Evolve 512 EMCCDs (pixel size: 16 µm x 16 µm), with two different aperture sizes. Decreasing the size of the aperture results in a decrease in measured luminescence intensity, while creating a more focussed image (e.g. Kook et al. 2015; Adamiec et al. 2025). TL, IRSL and $IRPL_{950}$ signals were detected using an aperture of 21.9 mm. The $IRPL_{900}$ signal was measured using an aperture of 21.9 mm ($IRPL_{900}$) and an aperture of 5 mm $IRPL_{900(highres)}$. This additional measurement of the $IRPL_{900}$ signal enables the effect of aperture size on the image quality to be assessed. A comparison of $IRPL_{900}$ measured with a 21.9 mm and a 5 mm aperture is presented in Fig. S1 in the supplementary material. Luminescence signals were measured using the measurement sequence outlined in Table 2. The samples were irradiated with a 100 Gy beta dose, prior to measuring $IRPL_{900}$ and IRL_{950} using a wide 21.9 mm aperture. These

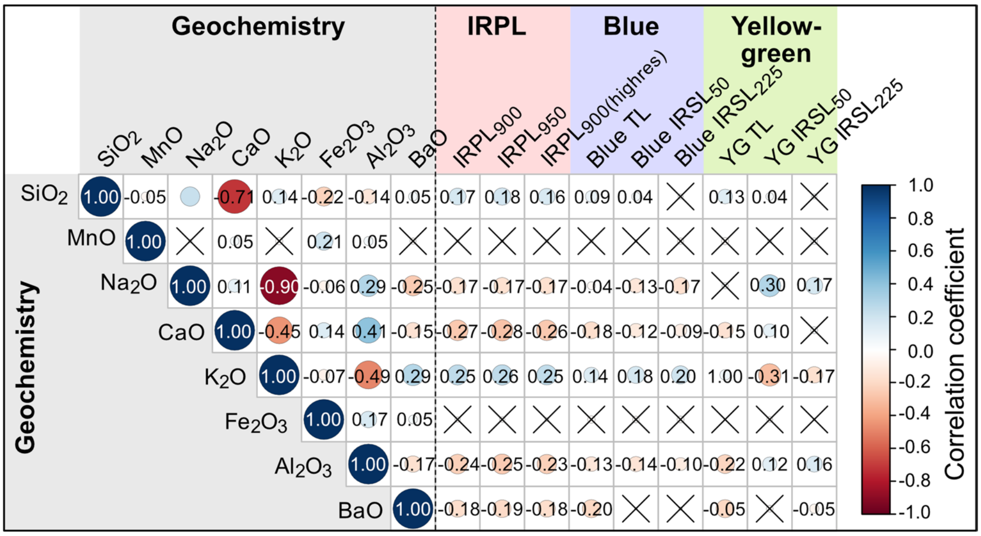

	Geochemistry								IRPL			Blue			Yellow-green		
	SiO_2	MnO	Na_2O	CaO	K_2O	Fe_2O_3	Al_2O_3	BaO	IRPL900	IRPL950	IRPL900(highres)	Blue TL	Blue IRSL50	Blue IRSL225	YG TL	YG IRSL50	YG IRSL225
SiO_2	1.00	-0.05		-0.71	0.14	-0.22	-0.14	0.05	0.17	0.18	0.16	0.09	0.04	×	0.13	0.04	×
MnO		1.00	×	0.05	×	0.21	0.05	×	×	×	×	×	×	×	×	×	×
Na_2O			1.00	0.11	-0.90	-0.06	0.29	-0.25	-0.17	-0.17	-0.17	-0.04	-0.13	-0.17	×	0.30	0.17
CaO				1.00	-0.45	0.14	0.41	-0.15	-0.27	-0.28	-0.26	-0.18	-0.12	-0.09	-0.15	0.10	×
K_2O					1.00	-0.07	-0.49	0.29	0.25	0.26	0.25	0.14	0.18	0.20	1.00	-0.31	-0.17
Fe_2O_3						1.00	0.17	0.05	×	×	×	×	×	×	×	×	×
Al_2O_3							1.00	-0.17	-0.24	-0.25	-0.23	-0.13	-0.14	-0.10	-0.22	0.12	0.16
BaO								1.00	-0.18	-0.19	-0.18	-0.20	×	×	-0.05	×	-0.05

Fig. 2 Correlation matrix of the oxide concentrations (wt%) and the intensity of the different luminescence signals gathered from 13 samples, by selecting areas of interest using line scans. All data was standardised prior to creating the correlation matrix. The correlation followed Pearson's product moment correlation coefficient. Black crosses indicate non-significant correlations, with $p > 0.01$. The yellow-green emission was abbreviated as YG in the signal labelling

Table 2 Measurement protocol used to obtain IRPL, TL and IRSL imaging results

Step	Detection unit	Treatment/settings	Obtained
1	-	Beta dose, ~100 Gy	
2	SIRIOL	830 nm laser stimulation (10 s) at room temperature, 21.9 mm aperture	IRPL$_{900}$
3	SIRIOL	830 nm laser stimulation (10 s) at room temperature, 21.9 mm aperture	IRPL$_{950}$
4	SIRIOL	830 nm laser stimulation (10 s) at room temperature, 5 mm aperture	IRPL$_{900(\text{highres})}$
5	DASH	Blue TL measurement to 250 °C for 60 s, heating rate of 5 °C s^{-1}	Blue (~400 nm) TL
6	DASH	Blue IRSL measurement at 50 °C for 100 s, heating rate of 2 °C s^{-1}	Blue (~400 nm) IRSL$_{50}$
7	DASH	Blue IRSL measurement at 225 °C for 100 s, heating rate of 2 °C s^{-1}	Blue (~400 nm) IRSL$_{225}$
8	DASH	Blue IRSL measurement at 290 °C for 100 s, heating rate of 2 °C s^{-1}	Background measurement
9	-	Beta dose, ~200 Gy	
10	SIRIOL	Steps 1–3	IRPL$_{900}$, IRPL$_{950}$, IRPL$_{900(\text{highres})}$
11	DASH	Yellow-green TL measurement to 250 °C for 60 s, heating rate of 5 °C s^{-1}	Yellow-green (~560 nm) TL
12	DASH	Yellow-green IRSL measurement at 50 °C for 100 s, heating rate of 2 °C s^{-1}	Yellow-green (~560 nm) IRSL$_{50}$
13	DASH	Yellow-green IRSL measurement at 225 °C for 100 s, heating rate of 2 °C s^{-1}	Yellow-green (~560 nm) IRSL$_{225}$
14	DASH	Yellow-green IRSL measurement at 290 °C for 100 s, heating rate of 2 °C s^{-1}	Background measurement
15	-	Repeat steps 4–14	

measurements were followed by an IRPL$_{900(\text{highres})}$ measurement using a 5 mm aperture. The protocol (Table 2) also contains measurements of TL to 250 °C (step 5 for blue TL and step 11 for yellow-green TL) and IRSL measurements at 50 °C and 225 °C (steps 6 and 7 for blue IRSL, and steps 12 and 13 for yellow-green IRSL). Since IRPL signals are difficult to optically reset (Winzar et al. 2025), samples were bleached twice in the protocol with IR light (steps 8 and 14) while being held at an elevated temperature (290 °C) (Kumar et al. 2021) in order to reset the IRPL signals.

Linking EMPA and luminescence data

The open-source image processing package Fiji (Schindelin et al. 2012) was used to integrate the luminescence signals from the EMCCD data after aligning different luminescence images. For further analysis, all frames acquired during the TL ramp and hold and during the 10 s IRPL measurement were summed, whilst for IRSL only the two frames that represent the initial 2 s of the decay curve were summed. Bright outliers were removed in Fiji using a median filter with a radius of 2 pixels and minimum threshold of 50 counts.

To be able to link the geochemistry and luminescence results, the visible images obtained after each luminescence measurement were used in combination with the electron backscatter images. Prominent features of the crystals, such as edges, corners or cracks were used to manually align the electron backscatter and visible images. From this alignment, transects of the luminescence data over the same distance as the EMPA line scans were selected in Fiji and exported for further processing. Since this was done manually, there will be some error in the registration. For this reason, only sufficiently large features were selected for luminescence and geochemical analysis. Fig. S2 presents a visualisation of this alignment process. Geochemical and luminescence transects were processed in R (R Core Team 2023), where the different resolution of luminescence (~20 µm) and EMPA data (5 µm, 10–20 µm) was overcome using a spline interpolation (spline(), R Core Team, 2023) to generate luminescence data at a spacing to match the resolution of the EPMA data.

Results

Correlations between geochemistry and luminescence

The major element chemistry results obtained using the EMPA and the spatially resolved luminescence measurements enable us to compare nine different luminescence emissions (IRPL$_{900}$, IRPL$_{950}$, IRPL$_{900(\text{highres})}$, blue (~400 nm) TL, blue (~400 nm) IRSL$_{50}$, blue (~400 nm) IRSL$_{225}$, yellow-green (~560 nm) TL, yellow-green(~560 nm) IRSL$_{50}$ and yellow-green (~560 nm) IRSL$_{225}$) with oxide concentrations of eight major elements (Si, Al, Mn, Na, Ca, K, Fe and Ba). In total we gathered 5350 interpolated data points for each parameter across 30 line scans over 13 samples. To get a better overview of this large dataset, we created a correlation matrix (Fig. 2). The matrix enables us to immediately spot correlations between two different variables, with negative correlations (one variable increases as the other variable decreases, represented by values from 0 to -1) displayed in red, and positive correlations (both variables show the same trend, both either increasing or decreasing, values range from 0 to 1) shown in blue (Fig. 2). The data was standardised prior to creating the correlation matrix using

Z scoring. Z scoring scales data by subtracting the average (μ) from each value (x) and dividing the result by the standard deviation (σ) : (equation: $x_{new} = (x - \mu)/\sigma$) to make them comparable regardless of their original unit. This standardisation transforms each data set in a way that it has an arithmetic mean of 0 and a standard deviation of 1. The correlation matrix was generated using the Pearson's product moment correlation coefficient. Only correlations with p-values < 0.01 were accepted and insignificant correlations are indicated by an X in the correlation matrix. The diagonal on the left side of Fig. 2 shows positive self-correlation between equivalent variables and are thus not considered further. Since the nine different luminescence signals investigated were stimulated and recorded using different light sources with different wavelengths and power densities, as well as with different detection setups, we refrain from directly comparing the intensities of these different emissions and have thus not included this comparison in the correlation matrix.

Geochemistry

There are positive and negative correlations between different oxides in the feldspar samples, representing well-known substitutions in the general feldspar chemistry. The negative correlations of Na_2O and K_2O (-0.90, Fig. 2) are due to the exchange of Na^+ and K^+, two cations with different ionic radii (e.g. Henderson 1986), resulting in the formation of perthitic lamellae during cooling of the feldspars (e.g. Parsons 1978; Deer et al. 2013; Parsons et al. 2015). The negative correlation between CaO and SiO_2 (-0.71) and between Al_2O_3 and SiO_2 (-0.14, see Fig. 2), results from the coupled substitution of.

$$Ca^{2+} + Al^{3+} \rightleftharpoons Na^+ + Si^{4+}, \tag{1}$$

which is necessary to maintain charge balance in the plagioclase solid solution. These ionic substitutions also explain the negative correlations between K_2O and CaO, and SiO_2 and Al_2O_3.

Furthermore, there exists a positive correlation between K_2O and BaO concentrations (0.29, see Fig. 2). In most feldspars, BaO is only present in sub percent quantities. Divalent Ba substitutes for K^+, and more rarely for Na^+ and Ca^{2+} (Deer et al. 2013). The substitution of K^+ by Ba^{2+} is possible due to their similar ionic radii (1.42 nm for Ba^{2+} and 1.51 nm for K^+, Henderson 1986), despite the difference in charge of these two cations, which is accommodated either by the following substitution (e.g. Gay and Roy 1968):

$$K^+ + Si^{4+} \rightleftharpoons Ba^{2+} + Al^{3+}. \tag{2}$$

Alternatively, the inclusion of Ba^{2+} for K^+ could result in vacancies on the alkali cation sites (e.g. Tas et al. 2025).

Geochemistry and luminescence

In terms of the relationships between measured oxide concentrations and IRPL signal intensity, IRPL emissions are positively correlated with K_2O (0.25 for $IRPL_{900}$ and 0.26 for $IRPL_{950}$) and SiO_2 concentrations (0.17 for $IRPL_{900}$ and 0.18 for $IRPL_{950}$), but negatively correlated with CaO (-0.27 for $IRPL_{900}$ and −0.28 for $IRPL_{950}$) and Al_2O_3 (-0.24 for $IRPL_{900}$ and −0.25 for $IRPL_{950}$), indicating higher IRPL intensities in alkali feldspars than plagioclase feldspars. IRPL emissions have no significant correlation with MnO and Fe_2O_3, and only a weak negative correlation exists between IRPL intensities and Na_2O concentrations (-0.17, Fig. 2). Blue TL, $IRSL_{50}$, and $IRSL_{225}$ emissions are weakly positively correlated with K_2O, and blue TL and $IRSL_{50}$ emissions are also weakly positively correlated with SiO_2 (0.09 and 0.04, respectively). All other oxides measured show weakly negative correlations with blue luminescence intensities and insignificant correlations with MnO and BaO (cf. Figure 2). For the yellow-green emissions, both IRSL signals are positively correlated with Na_2O (0.30 for $IRSL_{50}$ and 0.17 for $IRSL_{225}$) and negatively correlated with K_2O (-0.31 for $IRSL_{50}$ and −0.17 for $IRSL_{225}$). However, the yellow-green $IRSL_{50}$ signal is positively correlated to the CaO (0.10) and Al_2O_3 (0.12) concentrations, while the yellow-green TL signals are negatively correlated to these oxide concentrations (-0.15 and −0.05 for CaO and Al_2O_3, respectively, Fig. 2).

The correlation matrix shows that the oxide concentrations that appear to influence luminescence signal intensities are SiO_2 and Al_2O_3, which are both related to the structural framework of feldspar, and the cations K^+, Na^+, Ca^{2+} and Ba^{2+}, which are located at interstices in the structure. Strongest correlations occur with IRPL signals, and these relationships are explored further by dividing the dataset into alkali feldspars, macroperthites, and plagioclase feldspars, and plotting the intensity of IRPL against the oxide concentrations for these three data sets, with examples for K_2O and Na_2O shown in Fig. 3. Similar plots for the other feldspars and IRSL/TL signals are shown in Figures S2 to S12 in the supplementary material. There are no clear relationships between luminescence signal intensity and oxide concentration (e.g. Figure 3). Although Fig. 3a and c show that in alkali feldspars and macroperthites, respectively, areas with K_2O concentrations > 10 wt% contain three (or two) times as many $IRPL_{900}$ datapoints than areas with K_2O concentrations < 5 wt%, when looking at the measured $IRPL_{900}$ intensities, no clear trend can be seen with increasing K_2O

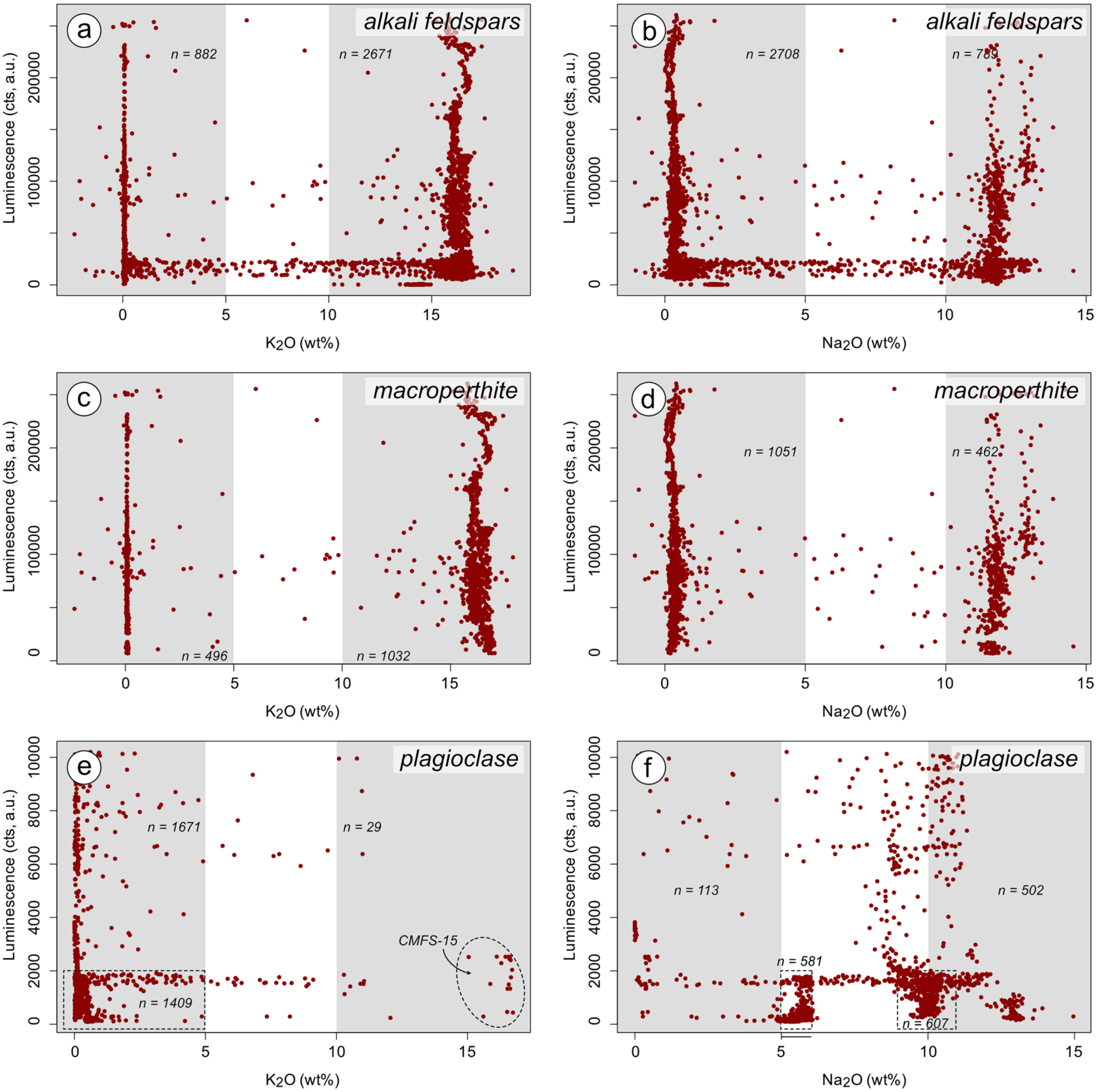

Fig. 3 Scatter plots of K_2O and Na_2O concentrations (wt%) compared to the $IRPL_{900}$ intensity. The dataset was divided into alkali feldspars only (a and b), macroperthites only (c and d) and plagioclase feldspars only (e and f). The shaded areas show measurement points with K_2O and Na_2O contents < 5 wt% and > 10 wt%. The number (n) of observations for each shaded area is given. The negative oxide concentrations visible in these figures are an artefact of the spline interpolation

concentration. Since K_2O and Na_2O are strongly negatively correlated (Fig. 2) the opposite picture emerges for Na_2O compared to IRPL. This indicates that the larger number of $IRPL_{900}$ emitting data points is only due to the subjective selection of measurement transects rather than actual trends of luminescence intensity and oxide concentration. This is due to the nature of feldspar exsolution, leading to the formation of two feldspars at subsolvus temperatures during crystallisation.

However, some scatter plots reveal interesting clusters of luminescence emissions at certain oxide concentrations: Fig. 3e for example, shows a cluster of $IRPL_{900}$ emitting data points at K_2O concentrations > 15 wt%. Figure S8e shows a concentration of $IRPL_{900}$ emitting data points at CaO concentrations of ~ 50 wt%, a chemical composition that indicates alteration of the feldspar sample. Similar clusters can be found in Fig. S10e and Fig. S11e for the blue and yellow-green TL signals, respectively. These clusters indicate that potentially interesting features could be observed on the individual transect or sample-level. The following sections will explore the spatially resolved luminescence signals with the EMPA transects in selected samples.

Spatially resolved luminescence

While the correlation matrix gives an overview of general trends, it cannot highlight specific features. Furthermore, principles of alkali feldspar exsolution limit the variety of chemical compositions and may thus mask effects of feldspar chemistry or structure on the luminescence intensities. To gain insights into smaller-scale chemical and luminescence features in feldspars, we will now explore the luminescence and geochemistry of alkali feldspars and plagioclases specifically selected as they either showcase common characteristics, such as perthite lamellae, or because they exhibit features, such as cracks or secondary mineral inclusions.

Alkali feldspars

From the correlation matrix it becomes evident that luminescence emissions in the IR, blue and yellow-green bands are related to the K-rich phases in the samples. These phases can be identified in the electron backscatter images of feldspars exhibiting macroperthitic lamellae (Fig. 4b and e). Directly comparing geochemical data and normalised $IRPL_{900}$ and $IRPL_{950}$ intensities (Fig. 4a and d) from line scans across the same areas of FSM-5 and CMFS-9 (Figs. 4c, f) reveals higher $IRPL_{900}$ and $IRPL_{950}$intensities with increasing K_2O concentrations (see grey shaded areas in Fig. 4c, f). Similarly to $IRPL_{900}$ and $IRPL_{950}$, but less pronounced, is the increase in normalised blue TL and yellow-green TL. Blue and yellow-green $IRSL_{50}$ and $IRSL_{225}$ emissions are more scattered, but follow the same trend as the TL emissions, at least for macroperthite CMFS-9 (Fig. 4f).

Clear trends as observed for macroperthites cannot be seen for all alkali feldspars. Depending on the type of alkali feldspar a different picture emerges. Sanidine sample CMFS-2, despite containing > 14 wt% of K_2O throughout the entire crystal, emits very low luminescence for all signals studied. Figure 5a shows the spatially resolved $IRPL_{900}$ signal for this most disordered sample (cf. Table S2). Contrary to what would be expected from the results of K-rich phases in macroperthites in Fig. 4, not the entire crystal emits luminescence. The luminescence (here: $IRPL_{900}$, Fig. 5a) is only concentrated around specific areas of the crystal. Whilst these areas do not show variations in major element chemistry (Figs. 5b, c), the electron backscatter image reveals the presence of multiple fractures throughout the sample (Fig. 5b, arrows indicate the location of the fractures), which in turn are defined by higher $IRPL_{900}$ and $IRPL_{950}$ emissions in those regions. Whilst $IRPL_{900}$ and $IRPL_{950}$ intensities seem to be strongly dependent on the presence of fractures, no such trend can be seen for the blue and yellow-green emissions (Fig. 5c).

Microperthite FSM-3 contains both, perthitic lamellae (on the µm-scale) and cracks. The dominant mineral phase of FSM-3 is microcline (78%), with albite only playing a minor role (22%) (Table 1). Overall, FSM-3 shows luminescence emissions in all three emission bands (IR, blue and yellow-green), with the edge of the crystal clearly visible in $IRPL_{900}$ and $IRPL_{950}$ profiles in Fig. 5f. Whilst luminescence emissions are present across the entire crystal, a linear feature, captured in the spatially resolved $IRPL_{900}$ (Fig. 5d) and the electron backscatter image (Fig. 5e), show the presence of a fracture. Similarly to CMFS-2, the $IRPL_{900}$ and $IRPL_{950}$ emission intensities increase across the fracture, whilst blue and yellow-green emissions do not seem to be affected by the presence of the fracture (Fig. 5f).

Thus, for alkali feldspars, luminescence emissions in the IR, blue and yellow-green emission bands are related to K-rich phases in macroperthites but not generally related to the presence of K_2O within a crystal (see CMFS-2, Fig. 5a). Furthermore, the presence of fractures influences the intensity of IRPL emissions in alkali feldspars (Fig. 5).

Plagioclase feldspars

A closer look at plagioclase feldspars indicates that in these minerals, other chemical and structural processes influence luminescence signal intensity (Figs. 6 and 7). Sample CMFS-16 (34.5% Ca-feldspar, Table 1) shows intense $IRPL_{900}$ emissions in one part of the crystal (cf. Figure 6a). The electron backscatter image, as well as SiO_2 and Al_2O_3 concentrations along a transect indicate that changes to the (Si, Al)-framework may be related to intense IRPL intensities. In contrast to the IRPL emissions, which seem to be enhanced by these changes to the framework, blue and yellow-green TL emission show a contrary effect, where intensity decreases in the affected regions (Fig. 6c).

Another part of the crystal shows both intense IRPL and intense yellow-green TL emissions (Fig. 6f). Here, the geochemical measurements reveal that this part of the crystal is dominated by high CaO contents (50 wt%). The remaining 50 wt% of the crystal's chemistry (H, C, O) in this area were not identifiable by the microprobe measurements, meaning that the other half of the crystal's composition is made up of elements other than those measured.

Fig. 4 Selected transects across macroperthites FSM-5 and CMFS-9. The IRPL$_{900}$ images (a, d) illustrate the change in IRPL$_{900}$ signal intensity with changes in feldspar chemistry due to perthite lamellae. The perthitic structure is especially visible in the electron backscatter images of FSM-5 (b) and CMFS-9 (e). The geochemical and luminescence data extracted from the measured and selected transects is shown in (c) and (f). The grey bars in (c) and (f) are aligned with high K$_2$O concentrations in the top graphs

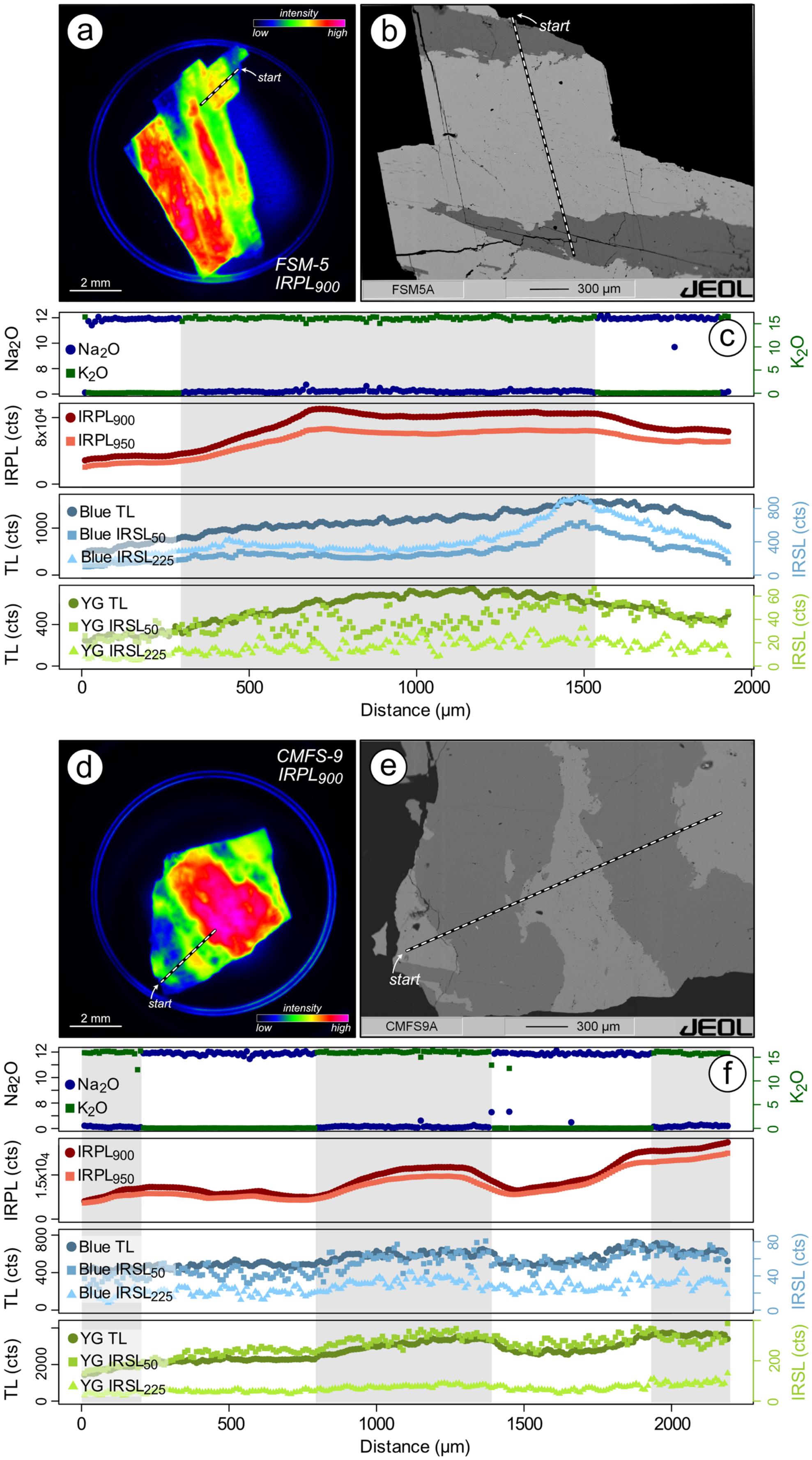

Plagioclase feldspars are more susceptible to weathering than alkali feldspars (e.g. Banfield and Eggleton 1990; White et al. 2001). The alteration features observed in CMFS-16 that suggest structural changes to the (Si, Al)-framework, are a typical pattern of silicate weathering with the transformation of albite to clay minerals, such as kaolinite or micas (e.g. White et al. 2001), with the weathering transformation from albite to kaolinite being described by:

$$NaAlSi_3O_8 + H^+ + \frac{9}{2}H_2O \rightarrow Na^+ + 2H_4SiO_4 + \frac{1}{2}Al_2Si_2O_5\left(OH\right)_4 \tag{3}$$

Furthermore, the CaO-rich area of CMFS-16 is likely defined by the re-precipitation of CaO in the crystal after fluid interactions, forming $CaCO_3$ phases through carbonation (e.g. Wawersik et al. 2001; Hangx and Spiers 2009; Munz et al. 2012):

$$CaAl_2Si_2O_8 + CO_2 + 2H_2O = CaCO_3 + Al_2Si_2O_5\left(OH\right)_4 \tag{4}$$

Other plagioclases and their luminescence features contribute to this complex picture. Albite CMFS-12 (0.67% Ca-feldspar), oligoclase CMFS-15 (20.5% Ca-feldspar), and labradorite CMFS-17 (59.9% Ca-feldspar) show different luminescence behaviour, despite all being part of the plagioclase solid solution. Whilst CMFS-12 (albite) shows very little luminescence at all (Fig. S23), CMFS-15 (oligoclase) shows intense luminescence emissions in all three emission bands (cf. Figures 7a, c). The areas of the sample, which emit the strongest luminescence in this oligoclase are areas with K-rich feldspar phases within the plagioclase matrix. The effect of this K-rich phase is most apparent in the IRPL emissions, but both blue and yellow-green TL emissions show an increase in luminescence intensity around these areas (cf. Figures 7a, c). CMFS-17 (labradorite) shows an interesting luminescence pattern: Whilst the sample shows no blue or yellow-green $IRSL_{50}$ and $IRSL_{225}$ emissions, it shows TL in both these emission windows across the entire crystal (cf. Figure 7f). $IRPL_{900}$ and $IRPL_{950}$ emissions are concentrated around fractures in the crystal (Fig. 7d, f), as seen for single phase sanidine CMFS-2 (cf. Figure 5a).

Altogether, plagioclase feldspars show a diverse picture of luminescence emissions: luminescence emissions are generally weaker in plagioclase feldspars compared to perthitic alkali feldspars, with very weak to no blue and yellow-green $IRSL_{50}$ and $IRSL_{225}$ emissions. IRPL emissions in plagioclases are either concentrated around fractures, K-rich inclusions, or around chemically weathered areas.

Discussion

IR emission (900 and 950 nm)

Spatially resolved IRPL measurements of 13 feldspars have shown that the luminescence emission in the IR region of the spectrum is most sensitive to structural as well as chemical changes to the crystal lattice compared to the two other emissions studied. Our results show that the presence of K-rich phases in both alkali feldspars (see macroperthites FSM-5 and CMFS-9 in Fig. 4) and plagioclases (see CMFS-15 in Fig. 7) results in more intense infrared emissions (900 and 950 nm), compared to Na_2O- or CaO-dominated areas of the crystal. The infrared emission is further enhanced by the presence of fractures in the crystal (see sanidine CMFS-2 in Fig. 5, or plagioclase CMFS-17 in Fig. 7). Alteration products, particularly visible in plagioclase feldspars (cf. CMFS-16, Fig. 6), also cause an increase in IR emissions.

Kumar et al. (2020) mapped CL emissions in the infrared and observed spatially variable emissions within a sediment sample and within individual grains of a single sample. While the emission at 955 nm is preferentially emitted from K-rich feldspars, moderately K- and Na-rich samples emit at 880 nm (Kumar et al. 2020). The instrumental setup used in the present study prevented us from measuring the 880 nm emission exactly, with the emission ~ 900 nm being recorded instead. This might hinder a direct comparison between the findings of Kumar et al. (2020) and the results in the present study. However, we also observe IR emissions recorded at 900 and 950 nm to be emitted by K-rich, as well as K-poorer alkali feldspars. The ubiquitous nature of IRPL in perthitic alkali feldspars contrasts with the more feature-oriented IRPL emission in the sanidine sample CMFS-2, as well as in plagioclase feldspars (cf. CMFS-12, CMFS-15, CMFS-16, and CMFS-17, cf. Figs. S20-S23).

It has been suggested that a defect located on the (Si, Al)-framework enables electron trapping (cf. Short 2004; Riedesel et al. 2019). A potential cause of the observed variability in IRPL intensity could be the different Si: Al ratio between alkali feldspars and plagioclases and the difference in Si^{4+} and Al^{3+} ordering on the framework between slowly-cooled microcline or orthoclase and rapidly-cooled sanidine. However, excitation-energy-dependent emission spectroscopy of a range of structurally different feldspars by Riedesel et al. (2021b) did not reveal any effects of framework disorder on the IRPL-emitting electron trapping centre characteristics, such as electron trap depth or IRPL emission wavelength. Another supporting argument for a framework position of the IRPL-emitting defect is the observation of intense IRPL emissions in altered regions of plagioclase feldspar CMFS-16 (cf. Figure 6a, Fig. S25). Here, the change of feldspar crystal to clay minerals and micas enhances the IRPL

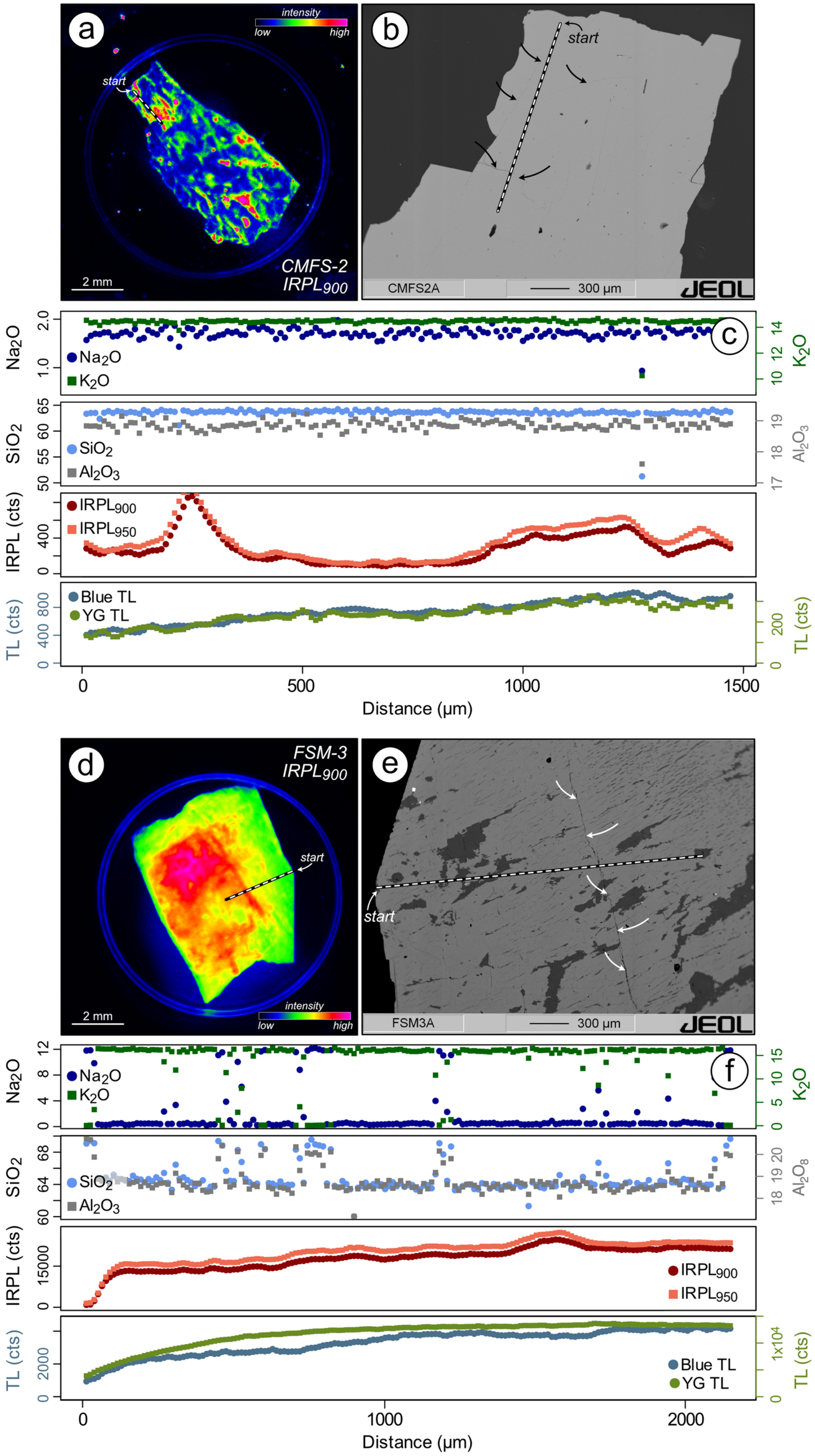
a
intensity
low
high
start
2 mm
CMFS-2
IRPL900
b
start
CMFS2A
300 µm
JEOL
c
Na2O
2.0
1.0
Na2O
K2O
K2O
14
12
10
SiO2
65
60
55
50
SiO2
Al2O3
Al2O3
19
18
17
IRPL (cts)
400
0
IRPL900
IRPL950
TL (cts)
800
400
0
Blue TL
YG TL
200
0
0
500
1000
1500
Distance (µm)
d
FSM-3
IRPL900
start
2 mm
intensity
low
high
e
start
FSM3A
300 µm
JEOL
f
Na2O
12
8
4
0
Na2O
K2O
K2O
15
10
5
0
SiO2
68
64
60
SiO2
Al2O3
Al2O3
20
19
18
IRPL (cts)
15000
0
IRPL900
IRPL950
TL (cts)
2000
0
Blue TL
YG TL
1x10^4
0
0
1000
2000
Distance (µm)

Fig. 5 Selected transects across alkali feldspars CMFS-2 (a-c) and FSM-3 (d-f). The spatially-resolved $IRPL_{900}$ image is shown for both samples (a, d), as well as the electron backscatter image (b, e). Selected geochemical and luminescence results are plotted along the transect (c, f). The small arrows indicate the location of fractures in the crystal

emission, compared to the non-altered part of the crystal. Interestingly, in this case the IRPL and blue emission intensities are anti-correlated.

We observed that $IRPL_{900}$ and $IRPL_{950}$ emissions increase around fractures within the crystal, supporting previous observations by Gunn et al. (2022). Fracturing of feldspars has been studied previously (e.g. Barnett and Kerrich 1980; Scheidl et al. 2014; Petrishcheva et al. 2019; Abart et al. 2022), and it has been shown that fracturing occurs due to stress (e.g. Rybacki et al. 2010), and that it can be chemically enhanced, leading to diffusion-induced crack propagation (e.g. Scheidl et al. 2014; Petrishcheva et al. 2019). Fractures in feldspars are susceptible to cation exchange and the diffusion of Na^+ and K^+ ions at the surface of the grain, when in contact with fluids (Scheidl et al. 2014; Petrishcheva et al. 2019). Electron backscatter images of fractures in plagioclase CMFS-17 (Fig. 7e) show variations in greyscale along the fractures, suggesting formation of secondary mineral phases along the crack walls. However, the analytical resolution chosen for the line scan across this area of CMFS-17 was too coarse to determine the chemical composition of the area around the fracture. This is also visible in the chemistry shown in Fig. 7f, where no changes to the oxide concentrations can be seen along the transect. Fractures in sanidine CMFS-2 (Fig. 5b) and perthite FSM-3 (Fig. 5e) do not show these changes to the brightness in the electron backscatter images. However, plagioclase CMFS-16 exemplifies how secondary mineral formation can occur along fractures, even leading to features of tens of micrometres in scale, and thus leading to intense emissions in the IR, as seen in Fig. 6d where $CaCO_3$ precipitation occurred in a plagioclase sample.

Blue luminescence (~ 400 nm)

It has often been suggested that the intensity of the blue (~400 nm) luminescence emission of feldspars is influenced by the K concentration of the samples (e.g. Spooner 1992; Prescott and Fox 1993; Huntley and Baril 1997). However, other studies have found no clear trend between the K concentration and the blue (~400 nm) IRSL intensity (e.g. Smedley et al. 2012; Maßon et al. 2024; Winzar et al. 2025). The spatially resolved luminescence results of alkali feldspars and plagioclase presented here also give an unclear picture of the relationship between K-concentration and blue luminescence intensity. Most alkali feldspars investigated show stronger blue luminescence than the plagioclase feldspars, but some very K-rich alkali feldspars emit only little luminescence at all (see CMFS-2). Weaker blue luminescence emissions in plagioclase feldspars, compared to alkali feldspars have been observed previously (e.g. Prescott and Fox 1993; Krbetschek and Rieser 1995; Riedesel et al. 2021a).

Less intense blue luminescence in plagioclase, with even weaker blue emissions in regions which are already transformed from feldspar to clay minerals, could be associated with a change to the crystal lattice: Whilst feldspars have a (Si, Al)-framework, the framework does not exist anymore in clay minerals, which are sheet silicates. Equation 1 shows the coupled substitution of Si^{4+} and Na^+ with Al^{3+} and Ca^{2+}, resulting in a Si: Al ratio of 2:2 in pure anorthite. Similarly, the transformation of albite to clay minerals, such as kaolinite (e.g. White et al. 2001; Eq. 3), affects the Si: Al ratio, changing it from 3:1 to 2:2. In the case of a Si: Al ratio of 2:2, the Al-Al avoidance rule governs the distribution of Al^{3+} ions on the framework, forbidding the presence of two neighbouring Al^{3+} ions (Löwenstein 1954; Finch and Klein 1999). The association of the blue luminescence emission with a hole centre on Al-bridging O ions (e.g. Speit and Lehmann 1982; Finch and Klein 1999; Riedesel et al. 2021a; Williams and Spooner 2025) could thus explain this data. In alkali feldspars, disorder of the framework can cause the presence of two neighbouring Al^{3+} ions, creating Al-O-Al bridges, with charges of Al^{3+}-O^--Al^{3+}, and thus a hole centre on the O ion. It is thus surprising that sanidine sample CMFS-2 is only weakly luminescent in the blue (Fig. 5a-c). Sanidine sample CMFS-2 does not show any blue $IRSL_{50}$ and only very weak $IRSL_{225}$ but shows TL emissions in the blue. Since this sample is a high temperature K-feldspar derivative with a disordered (Si, Al)-framework (see Table S2), intense blue luminescence would be expected (cf. Garcia-Guinea et al. 1999; Correcher et al. 2000; Riedesel et al. 2021a). Interestingly, Krbetschek and Rieser (1995), as well as Spooner et al. (2024), also found that their sanidine samples only emitted weak blue luminescence, similar to what is seen for CMFS-2 in the present study. A possible explanation for these contrasting observations is that CMFS-2 only shows weak luminescence emitted from electron retrapping ($IRPL_{900}$ and $IRPL_{950}$, Figs. 5, S11). This could potentially indicate a low density of defects acting as electron trapping centres. A low electron trap density would also hinder recombination-based luminescence processes such as $IRSL_{50}$ and $IRSL_{225}$. Winzar et al. (2025) similarly observed less intense blue IRSL emissions in disordered K-rich feldspars and attributed this to the influence of Al, Si ordering on lattice distortion. Increased ordering in triclinic feldspars enhances lattice strain, which may stabilise O^- centres on Al-O-Al bridges, enhance sub-conduction band transport through denser band-tail states, and/or broaden the distribution of trap-recombination centre distances relative to monoclinic feldspars. These effects may increase the accessibility of recombination centres during the IRSL process, and therefore the more intense blue luminescence observed in triclinic feldspars (e.g. microcline) compared to disordered monoclinic feldspars (e.g. sanidine) (Winzar et al. 2025).

Yellow-green emission (~ 560 nm)

The yellow-green emission (~560 nm) shows variable behaviour between the investigated samples. It is spatially heterogeneous in macroperthites (cf. Figure 4), as seen for IRPL, but it shows little spatial variability in microperthitic feldspars, such as FSM-3 (Fig. 5e) or CMFS-6 (Fig. S22). Contrasting to Baril (2004) who observed yellow-green IRSL primarily associated with Na-rich areas of feldspars, we recorded this emission in K-rich phases in alkali feldspars (e.g. CMFS-8 in Fig. S16), but also across the entire sample in plagioclase samples (e.g. plagioclase CMFS-15 in Fig. S24). The most interesting observation for the yellow-green emission is the localised emission in altered plagioclase CMFS-16 (Fig. 6d). Here, the secondary $CaCO_3$ mineral phase within the plagioclase sample emits intense yellow-green TL. This is not surprising, as bright yellow-green TL of (biogenic) calcite has been reported previously (Krbetschek et al. 1997; see their Table 7; Duller et al. 2009). As described for $IRPL_{900}$ and $IRPL_{950}$ in Sect. "IR emission (900 and 950 nm)", this $CaCO_3$ formation within the sample occurs within a fractured zone of the crystal. Leichmann et al. (2003) applied CL to study carbonatisation processes in plagioclase feldspars. Calcite phases emit orange CL (Leichmann et al. 2003), while we identify $CaCO_3$ luminescence signals in the infrared and yellow-green parts of the spectrum (cf. Figure 6), however, Leichmann et al. (2003) do not report any emission wavelength, thus it is unclear how different their CL emission is from the here reported TL and IRSL emissions. Carbonatisation of plagioclases (but also other feldspars) is a common occurrence when the fluids which cause the alteration of the feldspar contain high CO_2 partial pressure. Fluids rich in CO_2 react with the Ca from the plagioclase to form $CaCO_3$ (Leichmann et al. 2003; Munz et al. 2012).

With its weak $IRSL_{50}$ and $IRSL_{225}$ signal intensities, and spatially broad and featureless emission, the yellow-green emission is the least informative proxy.

Conclusion

In this study, we explored potential effects of a variety of chemical and structural features in alkali and plagioclase feldspars on the luminescence emissions recorded in the infrared (900 and 950 nm), blue (~400 nm), and yellow-green (~560 nm) regions of the spectrum to assess whether these signals could provide information on crystallisation or alteration products in feldspars. For our investigation, we used spatially resolved measurements of thermoluminescence, infrared stimulated luminescence, as well as infrared photoluminescence emissions, in combination with electron microprobe-based geochemical analyses of oxide concentrations and electron backscatter images. In total, we investigated the luminescence, geochemistry, and structural variety of 13 alkali feldspars and plagioclases.

We show that spatially resolved luminescence (IRPL, TL, $IRSL_{50}$, and $IRSL_{225}$) offers the potential to be used as a non-destructive, sensitive, and applicable tool for identifying spatially variable mineralogical and chemical features in feldspars. We observe that the infrared photoluminescence (IRPL) emission is the most sensitive to both chemical and structural variations in alkali feldspars and plagioclases. We found IRPL to be spatially related (i) to the presence of K-rich phases in macroperthitic alkali feldspars, but also to K-rich feldspar inclusions in plagioclases, (ii) to fractures within the crystal, and (iii) to alteration products such as clay minerals or $CaCO_3$ phases caused by fluid-interactions with the crystal.

The blue (~400 nm) luminescence signals, which are those most commonly used in luminescence dating studies and associated with a hole centre on Al-bridging O ions, is ubiquitous in perthitic alkali feldspars, but weak in sanidine and plagioclase samples. While in macroperthitic alkali feldspars, blue TL increases with the presence of K-rich perthite lamellae, in microperthitic alkali feldspars, the blue TL and IRSL emissions occur throughout the entire sample, indicating little spatial variability. In plagioclase feldspars, the blue emission is generally weak, with the TL signal being more prominent than the IRSL signals. In plagioclase samples, altered regions show less intense blue TL, whilst the IRPL emissions increase in such regions. Contact with fluids results in the formation of secondary minerals in plagioclase, such as calcite, emitting intense luminescence in the IR and yellow-green.

The results presented here demonstrate the sensitivity of three different luminescence emissions to variations in feldspar chemistry and structure. These relationships highlight the potential use of luminescence from feldspars to identify and quantify crystallisation and post-crystallisation processes in geological and petrological studies.

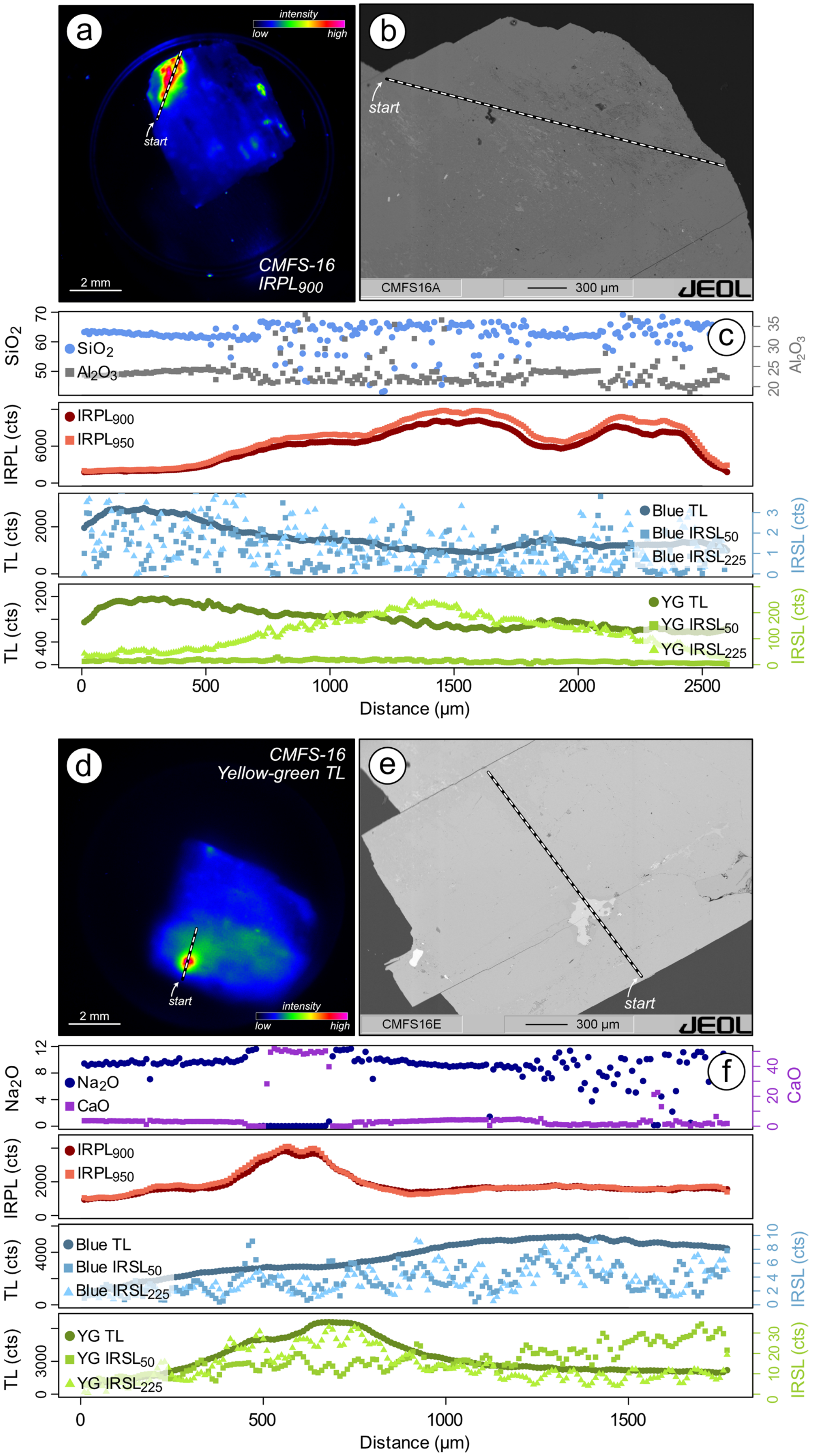

Fig. 6 Two selected transects across plagioclase feldspar CMFS-16. For the first transect the luminescence image ($IRPL_{900}$) is shown in (a), the electron backscatter image in (b) and selected geochemical and luminescence data in (c). The luminescence image (yellow-green TL) of the same shard with the second transect highlighted is shown in (d). An electron-backscatter image of the second transect is shown in (e) and selected geochemical data as well as luminescence results are given in (f). The grey bar in (c) highlights the part of the transect where alterations caused changes to SiO_2 and Al_2O_3 concentrations. In (f) the grey bar indicates the CaO-rich phase of the crystal. Please note the luminescence images in (a) and (d) show the same sample. The sample appears rotated due to the different relative location of the sample to the two EMCCD cameras detecting the $IRPL_{900}$ (a) and yellow-green TL signal (d)

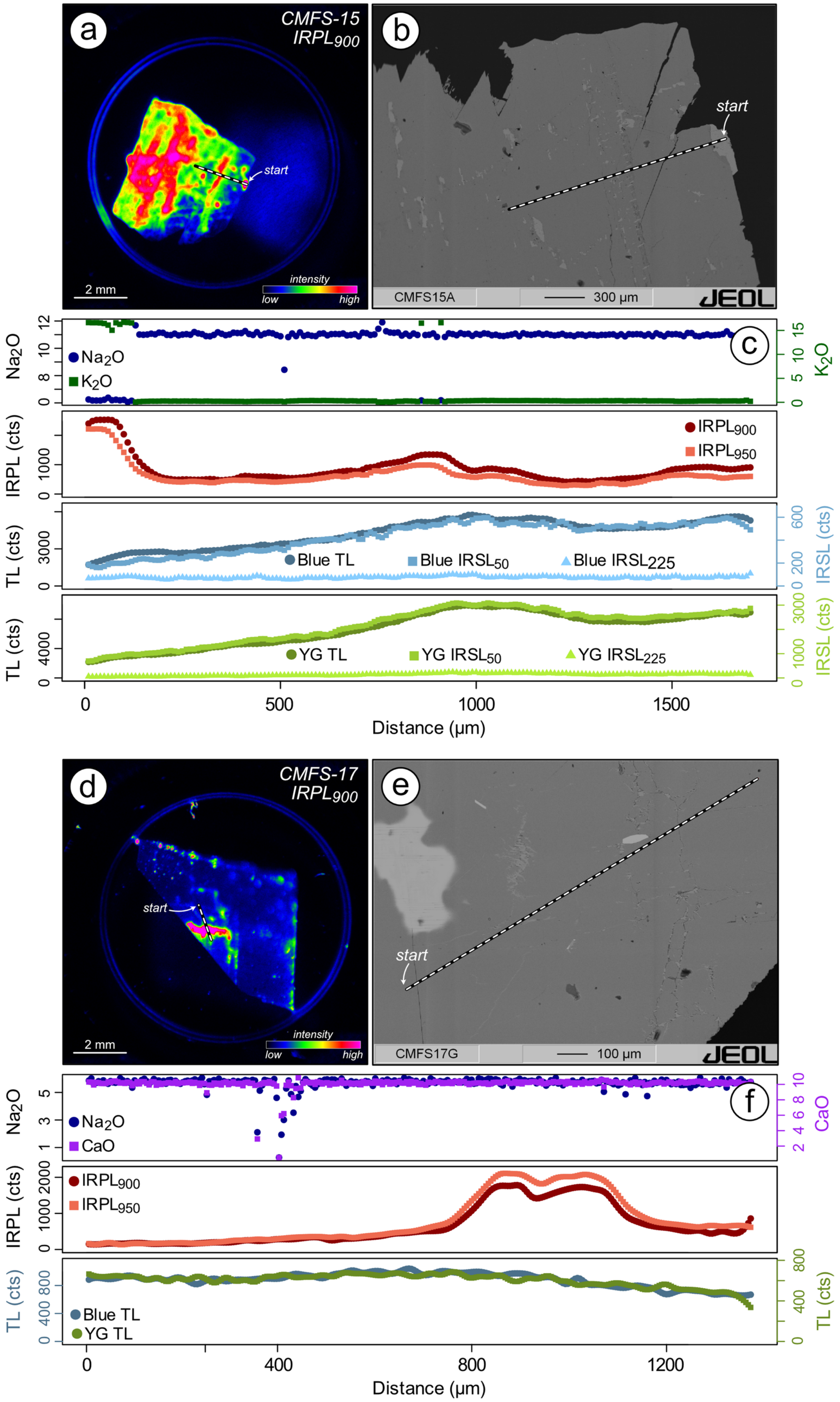
a
CMFS-15
IRPL900
start
2 mm
intensity
low
high
b
start
CMFS15A
300 µm
JEOL
c
Na2O
K2O
IRPL (cts)
IRPL900
IRPL950
TL (cts)
Blue TL
Blue IRSL50
Blue IRSL225
IRSL (cts)
YG TL
YG IRSL50
YG IRSL225
Distance (µm)
d
CMFS-17
IRPL900
start
2 mm
intensity
low
high
e
start
CMFS17G
100 µm
JEOL
f
Na2O
CaO
IRPL (cts)
IRPL900
IRPL950
TL (cts)
Blue TL
YG TL
Distance (µm)

Fig. 7 Spatially resolved IRPL_{900} luminescence, electron backscatter images and chemical as well as luminescence data for plagioclase samples CMFS-15 (a-c) and CMFS-17 (d-f)

Supplementary Information The online version contains supplementary material available at https://doi.org/10.1007/s00269-026-01345-z.

Acknowledgements Luminescence imaging at the Aberystwyth Luminescence Research Laboratory (ALRL) in Aberystwyth University forms part of the SPAtially Resolved geoChronology (SPARCL) initiative funded by HEFCW. SR would like to thank Dennis Wolf (University of Cologne) for slicing the feldspar samples and Kathrin Jung (University of Cologne) for preparing the epoxy pucks for electron microprobe measurements. The authors would like to thank Rolf Hollerbach (GeoMuseum, University of Cologne) for guiding in the selection of the CMFS samples and the GeoMuseum (University of Cologne) for providing them. We would like to thank two anonymous reviewers, whose comments helped us to improve the manuscript.

Author contributions SR: conceptualisation, methodology, data analysis, investigation, visualisation, and writing (original draft). GATD: conceptualisation, methodology, investigation, resources, writing review & editing. MH: methodology, investigation, writing—review & editing. NJGP: formal analysis, writing—review & editing. JAW: visualisation, writing—review & editing. AMTB: investigation, formal analysis, writing - review & editing. RK: methodology, investigation, resources, writing—review & editing.

Funding Open Access funding enabled and organized by Projekt DEAL. This research did not receive funding.

Data availability All data is available in the supplementary material.

Declarations

Conflict of interest The authors declare no competing interests.

References

Abart R, Petrishcheva E, Habler G, Sutter C, Fischer FD, Predan J, Kegl M, Rammerstorder FG (2022) Evolution of chemically induced cracks in alkali feldspar: thermodynamic analysis. Phys Chem Miner 49:13–15. https://doi.org/10.1007/s00269-022-01183-9

Adamiec G, Duller GAT, Gunn M (2025) Enhancing accuracy in EMCCD measurements of luminescence from single grains through minimising crosstalk. Geochronometria 52:205689. https://doi.org/10.20858/geochr/205689

Aitken MJ (1985) Thermoluminescence Dating. Academic, Oxford, p 385

Banfield JF, Eggleton R (1990) Analytical transmission electron microscopy of plagioclase, muscovite, and K-feldspar weathering. Clays Clay Minerals 38:77-89

Baril M (2004) CCD imaging of the infra-red stimulated luminescence of feldspars. Radiat Meas 38:81–86. https://doi.org/10.1016/j.radmeas.2003.08.005

Barnett RL, Kerrich R (1980) Stress corrosion cracking of biotite and feldspar. Nature 283:185–187. https://doi.org/10.1038/283185a0

Berner RA, Holdren GR (1977) Mechanism of feldspar weathering: Some observational evidence. Geology 5(6):369–372

Brantley SL, Shaughnessy A, Lebedeva MI, Balashov VN (2023) How temperature-dependent silicate weathering acts as Earth's geological thermostat. Science 379:382–389. https://doi.org/10.1126/science.add2922

Brown WL, Parsons I (1981) Towards a more practical two-feldspar geothermometer. Contrib Miner Petrol 76:369–377

Chardon ES, Livens FR, Vaughan DJ (2006) Reactions of feldspar surfaces with aqueous solutions. Earth Sci Rev 78:1–26. https://doi.org/10.1016/j.earscirev.2006.03.002

Correcher V, Garcia-Guinea J, Delgado A (2000) Influence of preheating treatment on the luminescence properties of adularia feldspar (KAlSi3O8). Radiat Meas 32:709–715

Cunningham GJ (1981) Petrology and Geochemistry of Lewisian Pegmatites and Granites, N.W., Scotland. PhD thesis, Imperial Collage London, United Kingdom

Deer WA, Howie RA, Zussman J (2013) An introduction to rock-forming minerals (3rd edition). Mineralogical Society, London, United Kingdom

Duan G, Ram R, Xing Y, Etschmann B, Brugger J (2021) Kinetically driven successive sonic and potassic alteration of feldspar. Nat Commun 12:4435. https://doi.org/10.1038/s41467-021-24628-1

Duller GAT (1997) Behavioural studies of stimulated luminescence from feldspars. Radiat Meas 27:663–694

Duller GAT (2004) Luminescence dating of Quaternary sediments: recent advances. J Quat Sci 19:183–192. https://doi.org/10.1002/jqs.809

Duller GAT, Bøtter-Jensen L, Markey (1997) A luminescence imaging system based on a CCD camera. Radiat Meas 27:91–99

Duller GAT, Penkman KEH, Wintle AG (2009) Assessing the potential for using biogenic calcites as dosemeters for luminescence dating. Radiat Meas 44:429–433

Finch AA, Klein J (1999) The causes and petrological significance of cathodoluminescence emissions from alkali feldspars. Contrib Miner Petrol 135:234–243

Frank MR, Fraley K, Kerwin S, Vaccaro D (2019) Feldspar-brine alteration at high-temperatures. Lithos 324–325:141–151. https://doi.org/10.1016/j.lithos.2018.10.029

Garcia-Guinea J, Townsend PD, Sanchez-Muñoz L, Rojo JM (1999) Ultraviolet-blue ionic luminescence of alkali feldspars from bulk and interfaces. Phys Chem Miner 26:658–667

Gay P, Roy NN (1968) The mineralogy of the potassium- barium feldspar series. III. Subsolidus relationships. Mineral Mag 36:914–932

Godfrey-Smith DI, Huntley DJ, Chen W-H (1988) Optical dating studies of quartz and feldspar sediment extracts. Q Sci Rev 7:373–380

Goldsmith JR, Laves F (1954) The microcline-sanidine stability relations. Geochim Cosmochim Acta 5:1–19

Gorelova LA, Vereshchagin OS, Bocharov VN, Krivovichev SV, Zolotarev AA, Rassomakhin MA (2023) CaAl2Si2O8 polymorphs: sensitive geothermometers and geospeedometers. Geosci Front 14:101458. https://doi.org/10.1016/j.gsf.2022.101458

Goudie AS, Viles HA (2012) Weathering and the global carbon cycle: geomorphic perspectives. Earth Sci Rev 113:59–71. https://doi.org/10.1016/j.earscirev.2012.03.005

Greilich S, Glasmacher UA, Wagner GA (2002) Spatially resolved detection of luminescence: a unique tool for archaeochronometry. Naturwissenschaften 89:371–375. https://doi.org/10.1007/s00114-002-0341-z

Gunn M, Duller GAT, Roberts HM (2022) SIRIOL: A Sensitive Infra-Red Instrument for phOto Luminescence measurements of feldspars. Radiat Meas 154:106182. https://doi.org/10.1016/j.radmeas.2022.106782

Hangx SJT, Spiers CJ (2009) Reaction of plagioclase feldspars with CO2 under hydrothermal conditions. Chem Geol 265:88–98. https://doi.org/10.1016/j.chemgeo.2008.12.005

Harlov DE, Hansen EC, Bigler C (1998) Petrologic evidence for K-feldspar metasomatism in granulite facies rocks. Chem Geol 151:373–386

Henderson P (1986) Inorganic geochemistry. Pergamon Press Ltd., Oxford, England

Hovis G (1989) Effect of Al-Si distribution on the powder-diffraction maxima of alkali feldspars and an easy method to determine T1 and T2 site occupancy. Can Mineral 27:107–118

Huntley DJ, Baril MR (1997) The K content of the K-feldspars being measured in optical dating or in thermoluminescence dating. Anc TL 15:3

Hütt G, Jaek I, Tchonka (1988) Optical dating: K-feldspars optical response stimulation spectra. Q Sci Rev 7:381–385

Jain M, Ankjærgaard C (2011) Towards a non-fading signal in feldspar: Insight into charge transport and tunnelling from time-resolved optically stimulated luminescence. Radiat Meas 46:292–309. 0.1016/j.radmeas.2010.12.004

Kayama M, Nakano S, Nishido H (2010) Characteristics of emission centres in alkali feldspar: A new approach by using cathodoluminescent spectral deconvolution. Am Mineral 95:1783–1795

Kook M, Lapp T, Mrray AS, Thomsen KJ, Jain M (2015) A luminescence imaging system for the routine measurement of single-grain OSL dose distributions. Radiat Meas 81:171–177. https://doi.org/10.1016/j.radmeas.2015.02.010

Krbetschek MR, Rieser U (1995) Luminescence spectra of alkalifeldspars and plagioclases. Radiat Meas 24:473–477

Krbetschek MR, Götze J, Dietrich A, Trautmann T (1997) Spectral information from minerals relevant for luminescence dating. Radiat Meas 27:695–748

Kroll H, Evangelakakis C, Voll G (1993) Two-feldspar geothemometry: a review and revision for slowly cooled rocks. Contrib Miner Petrol 114:510–518

Kumar R, Martin LIDJ, Poelman D, Vandenberghe D, De Grave J, Mook M, Jain M (2020) Site-selective mapping of metastable states using electron-beam induced luminescence microscopy. Sci Rep 10(15650). https://doi.org/10.1038/s41598-020-72334-7

Kumar R, Kook M, Jain M (2021) Sediment dating using infrared photoluminescence. Quat Geochronol 62:101147. https://doi.org/10.1016/j.quageo.2020.101147

Lapp T, Kook M, Murray AS, Thomsen KJ, Buylaert J-P, Jain M (2015) A new luminescence detection and stimulation head for the Risø TL/OSL reader. Radiat Meas 81:178–184. https://doi.org/10.1016/j.radmeas.2015.02.001

Leichmann J, Broska I, Zachovalová K (2003) Low-grade metamorphic alteration of feldspar minerals: a CL study. Terra Nova 15:104–108

Löwenstein W (1954) The distribution of aluminium in the tetrahedra of silicates and aluminates. American Mineralogist 39:92-96

Maßon LAE, Riedesel S, Zander A, Sontag-González M, Reimann T (2024) Testing the applicability of standardised growth curves for chemically heterogeneous single-grain feldspars from the Atacama Desert, Chile. Quat Geochronol 83:101585. https://doi.org/10.1016/j.quageo.2024.101585

Munz IA, Brandvoll Ø, Haug TA, Iden K, Smeets R, Kihle J, Johansen K (2012) Mechanisms and rates of plagioclase carbonate reactions. Geochim Cosmochim Acta 77:27–51. https://doi.org/10.1016/j.gca.2011.10.036

Parsons I (1978) Feldspars and fluids in cooling plutons. Mineral Mag 42:1–17

Parsons I, Gerald F, J. D., and, Lee MR (2015) Routine characterization and interpretation of complex alkali feldspar intergrowths. Am Mineral 100:1277–1303

Petrishcheva E, Rieder M, Predan J, Ficher FD, Giester G, Abart R (2019) Diffusion-controlled crack propagation in alkali feldspars. Phys Chem Miner 46:15–26. https://doi.org/10.1007/s00269-018-0983-9

Poolton NRJ, Kars RH, Wallinga J, Bos AJJ (2009) Direct evidence for the participation of band-tails and excited-state tunnelling in the luminescence of irradiated feldspars. J Phys: Condens Matter 21:485505. https://doi.org/10.1088/0953-8984/21/48/485505

Prasad AK, Poolton NRJ, Kook M, Jain M (2017) Optical dating in a new light: A direct, non-destructive probe of trapped electrons. Sci Rep 7:12097. https://doi.org/10.1038/s41598-017-10174-8

Prescott JR, Fox PJ (1993) Three-dimensional thermoluminescence spectra of feldspars. J Phys D: Appl Phys 26:2245–2254. https://doi.org/10.1088/0022-3727/26/12/024

R Core Team (2023) R: A language and environment for statistical computing. R Foundation for Statistical Computing, Vienna, Austria

Reed SJB (2005) Electron Microprobe Analysis and Scanning Electron Microscopy in Geology, 2nd edn. Cambridge University Press

Rhodes EJ (2011) Optically stimulated luminescence dating of sediments over the past 200,000 years. Annual reviews Earth Planet Sci 39:461–488. https://doi.org/10.1146/annurev-earth-040610-133425

Richter DK, Götte T, Götze J, Neuser RD (2003) Progress in application of cathodoluminescent (CL) in sedimentary petrology. Mineral Petrol 79:127–166

Riedesel S, King GE, Prasad AK, Kumar R, Finch AA, Jain M (2019) Optical determination of the width of the band-tail states, and the excited and ground state energies of the principle dosimetric trap in feldspar. Radiat Meas 125:40–54. https://doi.org/10.1016/j.radmeas.2018.08.019

Riedesel S, Bell AMT, Duller GAT, Finch AA, Jain M, King GE, Pearce NJ, Roberts HM (2021a) Exploring sources of variation in thermoluminescence emissions and anomalous fading in alkali feldspars. Radiat Meas 141:106541. https://doi.org/10.1016/j.radmeas.2021.106541

Riedesel S, Kumar R, Duller GAT, Roberts HM, Bell AMT, Jain M (2021b) Site-selective characterisation of electron trapping centres in relation to chemistry, structural state and mineral phases present in single crystal alkali feldspars. J. Phy. D: Appl. Phys. 54, 385107. https://doi.org/10.1088/1361-6463/ac10d7

Riedesel S, Duller GAT, Ankjærgaard C (2023) Time-resolved infrared stimulated luminescence of the blue and yellow-green emissions – Insights into charge recombination in chemically and structurally different alkali feldspars. J Lumin 257:119724. https://doi.org/10.1016/j.jlumin.2023.119724

Rybacki E, Wirth R, Dresen G (2010) Superplasticity and ductile fracture of synthetic feldspar deformed to large strain. J Geophys Res 115:B08209. https://doi.org/10.1029/2009JB007203

Scheidl KS, Schaeffer A-K, Petrishcheva E, Habler G, Fischer FD, Schreuer J, Abart R (2014) Chemically induced fracturing in alkali feldspars. Phys Chem Miner 41:1–16. https://doi.org/10.1007/s00269-013-0617-1

Schindelin J, Arganda-Carreras I, Frise E, Kaynig V, Longair M, Pietzsch T, Preibisch S, Rueden C, Saalfeld S, Schmid B, Tinevez

JY (2012) Fiji: an open-source platform for biological-image analysis. Nat Methods 9(7):676–682

Short MA (2004) Determining the possible lattice sites of two unknown defects in orthoclase from the polarization effects in their optical transitions. J Phys : Condens Matter 16:7405–7417

Smedley RK, Duller GAT, Pearce NJG, Roberts HM (2012) Determining the K-content of single-grains of feldspar for luminescence dating. Radiation Measurements, Proceedings of the 13th International Conference on Luminescence and Electron Spin Resonance Dating, 10–14 July, 2011, Toruń, Poland 47, 790–796. https://doi.org/10.1016/j.radmeas.2012.01.014

Speit B, Lehmann (1982) Radiation defects in feldspars. Phys Chem Miner 8:77–82. https://doi.org/10.1007/BF00309017

Spooner NA (1992) Optical dating: Preliminary results on the anomalous fading of luminescence from feldspars. Quaternary Science Reviews, Proceedings of the 6th International Specialist Seminar on Thermoluminescence and Electron Spin Resonance Dating 11, 139–145. https://doi.org/10.1016/0277-3791(92)90055-D

Spooner NA, Williams OW, Questiaux DG (2024) Pulsed infrared stimulated luminescence measurements for defect pair model studies in feldspars. Radiat Meas 170:107044. https://doi.org/10.1016/j.radmeas.2023.107044

Stormer JC Jr. (1975) A practical two-feldspar geothermometer. Am Mineral 60:667–674

Tas B, Gorfer A, Petrishcheva, Wilde G, Abart R, Divinski S (2025) Sodium diffusion in alkali feldspars: towards the impact of Al/Si ordering. Phil Mag 1–16. https://doi.org/10.1080/14786435.2025.2531527

Thompson JB, JR (1969) Chemical reactions in crystals. Am Mineral 54:341–375

Thompson JB, JR (1970) Chemical reactions in crystals: corrections and clarification. Am Mineral 55:528–532

Thomsen KJ, Murray AS, Jain M, Bøtter-Jensen L (2008) Laboratory fading rates of various luminescence signals from feldspar-rich sediment extracts. Radiat Meas 43:1474–1486. https://doi.org/10.1016/j.radmeas.2008.06.002

Thomsen KJ, Kook M, Murray AS, Jain M (2018) Resolving luminescence in spatial and compositional domains. Radiat Meas 120:260–266. https://doi.org/10.1016/j.radmeas.2018.06.002

Ussher WAE, Barrow G, McAlister DA (1909) The Geology of the Country Around Bodmin and St. Austell. Memoirs of the Geological Survey England and Wales. – Explanation Sheet 347, 182-185.

Huntley DJ, Godfrey-Smith DI, Thewalt MLW (1985) Optical dating of sediments. Nature 313:105-107

Hellmann, R., Zhai, Y., Robin, E., Findling, N., Mayanna, S., Wirth, R., Schreiber, A., Cabié, M., Zeng, Q., Liu, S., Liu, J., 2021. The hydrothermal alkaline alteration of potassium feldspar: A nanometer-scale investigation of the orthoclase interface. Chemical Geology 569, 120133. https://doi.org/10.1016/j.chemgeo.2021.120133

Wawersik WR, Rudnicki JW, Dove P, Harris J, Logan JM, Pyrak-Nolte L, Orr FM Jr., Ortoleva PJ, Richter F, Warpinski NR, Wilson JL, Wong T-F (2001) Terrestrial sequestration of CO2: an assessment of research needs. Adv Geophys 43:97–177

White AF, Bullen TD, Schulz MS, Blum AE, Huntington TG, Peters NE (2001) Differential rates of feldspar weathering in granitic regoliths. Geochim Cosmochim Acta 65(6):847–869. https://doi.org/10.1016/S0016-7037(00)00577-9

Williams OM, Spooner NA (2025) Charge carrier release mechanisms underlying the emission of alkali feldspar infrared stimulated luminescence. Radiat Meas 181:107362

Winzar JA, Duller GAT, Roberts HM, Gunn M, Bell AMT (2025) Intensity and optical resetting of Infrared Photoluminescence (IRPL) and Infrared Stimulated Luminescence (IRSL) signals in feldspars. J Lumin 278:121018. https://doi.org/10.1016/j.jlumin.2024.121018

Yuan G, Cao Y, Schulz H-M, Hao F, Gluyas J, Liu K, Yang T, Wang Y, Xi K, Li F (2019) A review of feldspar alterations and its geological significance in sedimentary basins: From shallow aquifers to deep hydrocarbon reservoirs. Earth Sci Rev 191:114–140. https://doi.org/10.1016/j.earscirev.2019.02.004